Analyst

PAPER

View Article Online
View Journal

Cite this: DOI: 10.1039/c9an01631g

A fingerprint of amyloid plaques in a bitransgenic animal model of Alzheimer's disease obtained by statistical unmixing analysis of hyperspectral Raman data

Emerson A. Fonseca,*[a] Lucas Lafetá,[a] Renan Cunha,[a] Hudson Miranda,[b] João Campos,[a] Helton G. Medeiros,[c] Marco A. Romano-Silva,[d] Raigna A. Silva,[a,e] Alexandre S. Barbosa,[a,f] Rafael P. Vieira,[g] Leandro M. Malard[a] and Ado Jorio*[a]

Received 23rd August 2019,
Accepted 13th October 2019

DOI: 10.1039/c9an01631g

rsc.li/analyst

The global prevalence of Alzheimer's disease (AD) points to endemic levels, especially considering the increase of average life expectancy worldwide. AD diagnosis based on early biomarkers and better knowledge of related pathophysiology are both crucial in the search for medical interventions that are able to modify AD progression. In this study we used unsupervised spectral unmixing statistical techniques to identify the vibrational spectral signature of amyloid β aggregation in neural tissues, as early biomarkers of AD in an animal model. We analyzed spectral images composed of a total of 55 051 Raman spectra obtained from the frontal cortex and hippocampus of five bitransgenic $APP_{swe}PS1_{\Delta E9}$ mice, and colocalized amyloid β plaques by other fluorescence techniques. The Raman signatures provided a multifrequency fingerprint consistent with the results of synthesized amyloid β fibrils. The fingerprint obtained from unmixed analysis in neural tissues is shown to provide a detailed image of amyloid plaques in the brain, with the potential to be used as biomarkers for non-invasive early diagnosis and pathophysiology studies in AD on the retina.

Introduction

Global average life expectancy has increased in the last few decades, followed by a remarkable increase in the prevalence of age-related chronic diseases. Neurodegenerative disorders are highlighted among these, especially Alzheimer's disease (AD), the most severe and disabling form of dementia.[1] Due to the progressive neurodegeneration related to AD, as well as the limited impact of medical interventions in already disabled AD patients, there is a worldwide effort in establishing biomarkers for early AD diagnosis.[2,3] The histopathological hallmarks of AD, the extracellular depositions of misfolded amyloid-beta peptide (Aβ) forming amyloid plaques associated with neurofibrillary tangles, are the major subjects of investigation in AD diagnosis and pathophysiology.[4]

Raman spectroscopy, a technique based on the inelastic scattering of light by molecules, is a marker-free, widely used tool for identifying and characterizing biomaterials and biological tissues.[5,6] However, tissues are composed of a mixture of distinct biomolecules,[7] exhibiting a very complex Raman spectral signature that also depends on environmental conditions. In this context, identifying the spectral fingerprint of specific biomolecular structures in a biomedical relevant environment is challenging. The objective of this work is to establish a robust multifrequency Raman based fingerprint for the identification and compositional analysis of amyloid plaques.

Dong *et al.* characterized amyloid plaque cores from the human brain with Raman microscopy;[8] Chen *et al.* performed a similar analysis from the rat brain after injection of the $A\beta_{25-35}$ peptide into the hippocampus;[9] a frequency blue-shift in the amide I Raman feature has been established as the main biomarker in amyloid plaque identification. Later, R. Michael *et al.* successfully imaged optically amyloid plaques in the human brain using a hyperspectral Raman technique.[10] In a recent study using the APP/PS1 bitransgenic mice brain, stimulated Raman spectroscopy (SRS) exhibited the blue-shifted amide I frequency at 1670 cm^{-1}.[11]

[a]Departamento de Física, ICEx, UFMG, Belo Horizonte, MG, 31270-901, Brazil. E-mail: adojorio@fisica.ufmg.br
[b]Programa de Pós-Graduação em Engenharia Elétrica, UFMG, Belo Horizonte, MG, 31270-901, Brazil
[c]Divisão de Metrologia de Materiais, Instituto Nacional de Metrologia Qualidade e Tecnologia (Inmetro), 25250-020 Duque de Caxias, RJ, Brazil
[d]Departamento de Saúde Mental-Faculdade de Medicina, UFMG, Belo Horizonte, MG, 30130-100, Brazil
[e]Instituto de Física, UFU, Uberlândia, MG, 38400-920, Brazil
[f]Departamento de Oftalmologia, Faculdade de Medicina, HC/UFMG, Belo Horizonte, MG, 30130-100, Brazil
[g]Departamento de Bioquímica e Imunologia, UFMG, CEP 30161-70 Belo Horizonte, Minas Gerais, Brazil

Here we characterize amyloid plaques in brain tissues from an $APP_{swe}PS1_{\Delta E9}$ AD mouse model using a hyperspectral Raman imaging technique and study the massive set of Raman data using unsupervised unmixing spectral analysis. The main aim of this work is to analyze and to comprehensibly demonstrate how the multifrequency set of vibration modes comprise a fingerprint to consistently identify amyloid plaques in the AD mice brain, paving the way to validate Raman imaging as an accurate method in amyloid plaque identification and study in neural tissues. The importance of this result resides on the fact that the optical identification of Aβ aggregation in amyloid plaques located in neural tissues could be extended to the retina, proposed as an inexpensive and non-invasive early AD diagnosis method,[12–14] due to the transparency of anterior ocular structures (cornea and lens) and the high synaptic density of its plexiform layers.[15]

Experimental results

Characterization of amyloid beta fibrils

Before performing Raman imaging on tissues, we prepared synthetic fibrils for Raman spectroscopy characterization using an adapted incubation protocol.[16] Fibril-like structure formation was confirmed by Atomic Force Microscopy (AFM) (Fig. 1A) and by Transmission Electronic Microscopy (TEM) (Fig. 1B). Fig. 1C shows (red trace) the characteristic Raman spectrum for the $A\beta_{1-42}$ fibrils. For a comparison purpose, Fig. 1C also shows (blue trace) the Raman spectrum of bovine serum albumin (BSA) which contains about 55% α helix and 45% disordered structures.[17]

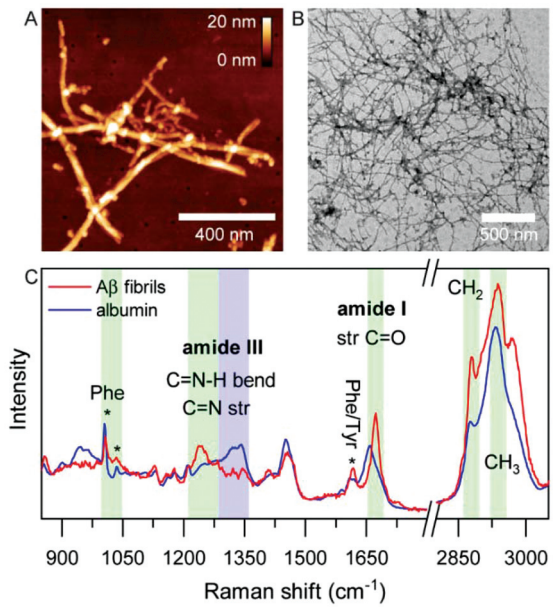

Fig. 1 Characterization of synthetic amyloid-β (Aβ) fibrils. (A) AFM and (B) TEM images of synthetic Aβ fibrils. (C) Raman spectra of synthetic Aβ fibrils (red) and bovine serum albumin (BSA) (blue). Raman peaks important for β sheet identification are highlighted in green. Amide I shows a frequency blue-shift in Aβ fibrils (1672 cm^{-1}) and amide III a red-shift (centered at 1233 cm^{-1}) when compared with BSA amide I (1658 cm^{-1}) and amide III (1310 cm^{-1}). Amide III for the β sheet is highlighted in green, while for the α helix it is highlighted in purple. The three asterisks point to the Phe bands at 1007 cm^{-1} and 1036 cm^{-1}, and the overlapped Phe at 1609 cm^{-1} and Tyr at 1612 cm^{-1}.

Hyperspectral Raman measurement

In order to characterize the spectral Raman fingerprint that could be used as a reference for *in vivo* conditions, tissues were prepared for assays following a minimum of sample preparation. Cryosection was kept as the only standard procedure. Prior to staining, amyloid plaques were Raman scanned, preventing an overlap by the fluorescent dye. The experiment workflow followed the sequence: amyloid plaque visualization by autofluorescence (Fig. 2A); optical image on the same region of interest (ROI) (Fig. 2B); Raman hyperspectral mapping acquisition (Fig. 2C); ThioS staining for the confirmation of amyloid plaques (Fig. 2D); and data analysis (Fig. 2E, 3 and 4). Snap-frozen, 80 μm thick slices of perfused 6-month-old $APP_{swe}PS1_{\Delta E9}$ mice (4 Tg mice) showed an intense plaque autofluorescence signal (*e.g.* Fig. 2A), following established procedures.[18,19] After TPEF identification, the slices were analyzed with Raman hyperspectral imaging. The mapped area ranged from 25 × 25 μm^2 to 240 × 240 μm^2, with step sizes of 1.2 μm (low spatial resolution) and 500 nm (high spatial resolution), and a spectral resolution of 2.45 cm^{-1}. The green excitation chosen (532 nm wavelength) proved to be ideal for improved Raman efficiency in our biological samples, with an optimized signal-to-noise ratio.[19]

Amyloid plaque imaging

Unsupervised spectral unmixing analysis of the hyperspectral data was performed, and each data set (each plaque image) was loaded separately to the spectral unmixing algorithm. As an output, we obtained the most dissimilar spectra, established as end members (EMs) in the data set. Fig. 2E shows one example, from one data set, of the EM spectra obtained, which corresponds to the spectra of the background (EM1), the surrounding tissue (EM2) and the amyloid plaque (EM3). The same procedure was carried out for all the amyloid plaque samples studied in this work (Fig. 3 and 4). Raman spectra were analysed at 18 different amyloid plaques and surrounding areas, located in two regions of the brain (hippocampus and frontal cortex), from 5 different mice: four mice of 6 months of age for low spatial resolution imaging (Fig. 3), and one of 12 months of age for high spatial resolution imaging (Fig. 4). Here we report the results from a total of 55 051 spectra obtained from 7 plaque regions. In the latter (12 months mouse), five EMs were obtained, but only three are shown in Fig. 4, where the EM for the background and an alternative EM for the plaque identification are not discussed.

Discussion

A spectroscopic fingerprint of amyloid β fibrils

Amyloid plaques are extracellular depositions of misfolded amyloid-beta peptide (Aβ), mostly $A\beta_{1-40}$ and $A\beta_{1-42}$ species.

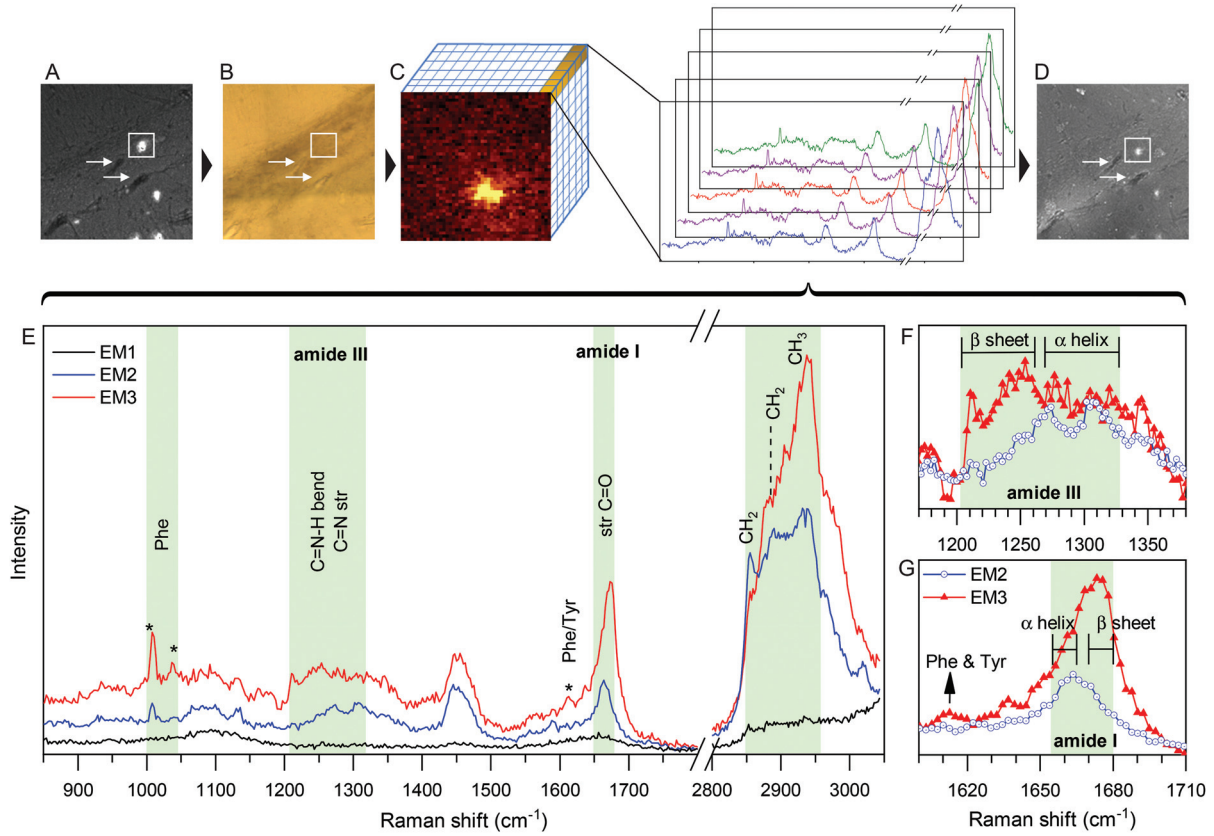

Fig. 2 Hyperspectral Raman imaging of the AD mice brain section and the spectral unmixing analysis. (A) Autofluorescence image of the amyloid plaque in a frontal cortex brain slice. (B) Optical image of the same region in (A). White arrows indicate tissue profiles utilized for optical co-localization. (C) Hyperspectral Raman data acquisition in the squared location in (A) and (B). (D) ThioS staining. (E) Results of spectral unmixing analysis showing three end members (EMs): black, blue and red EM spectra are the fingerprint of the background, the surrounding tissue and the amyloid plaque, respectively. Amide III presents a red-shift (centered at 1233 cm^{-1}, highlighted in (F)); amide I shows a blue-shift (1675 cm^{-1}, highlighted in (G)). The three asterisks point to the Phe bands at 1007 cm^{-1} and 1036 cm^{-1}, and the overlapped Phe at 1609 cm^{-1} and Tyr at 1612 cm^{-1}. The high-frequency CH stretching regions of CH_2 (~2854 cm^{-1}) and CH_3 (~2930 cm^{-1}) bands were associated with lipids and proteins/lipids, respectively.

These aggregates present a β-pleated sheet conformation, well stabilized by hydrophobic interactions and hydrogen bonding.[16] Aβ peptide monomers derived from transmembrane protein cleavage of the amyloid precursor protein (APP) form oligomers, intermediary neurotoxic structures which aggregate producing amyloid fibrils and plaques.[4,20] The amyloid aggregating process has been correlated to tau pathology, characterized by tau neurofibrillary tangles of microtubule-associated proteins, as well as neurodegeneration and neuronal death.[4,21]

According to the literature, amyloid plaques in brain tissues have been analyzed with different spectroscopic methods and protocols. Molecular identifications and characterization are based here on the Raman effect, a highly accurate and label-free method according to which incident light is scattered by exchanging energy with molecular vibrations in the sample. Distinct patterns of light scattering related to specific molecular modes of vibration provide a vibration-based molecular identification. Raman spectroscopy identifies the α helix and the β sheet secondary structures of proteins and peptides[22–25] and is also used for the characterization and distribution of lipids[26,27] in tissue samples.[6,28,29] It has been shown that the amide I vibration, which is associated with C═O stretching in the peptide backbone, is subjected to different restoring forces in the α helix and β sheet.[30] Studies have also shown the vibrational fingerprint of proteins, peptides, and amino acid structures by Fourier transform infrared micro-spectroscopy (μFTIR),[30,31] as well as amyloid plaques in brain tissues from AD transgenic mice.[32,33] However, IR spectroscopy has limited applicability for spectroscopic imaging in an aqueous medium and dispersive Raman scattering microscopy, unlike μFTIR, achieves higher spatial resolution due to the smaller excitation wavelength in both dried and wet samples, which can be studied with relatively simple sample preparation. Given the superior specificities of Raman spectroscopy compared to other techniques, it has been chosen in many studies exploring chemical, biochemical and histological mapping of various tissues,[5,19,34,35] providing valuable label-free and non-destructive data in AD neurodegeneration.[10,11,36]

The Aβ peptide vibrational modes are mainly composed of C═O, C–H, C–N and amino acid side chains. The peptide/protein folding, *e.g.* α helix and β sheet, results in the characteristic amide I peak, which is established as the most accurate

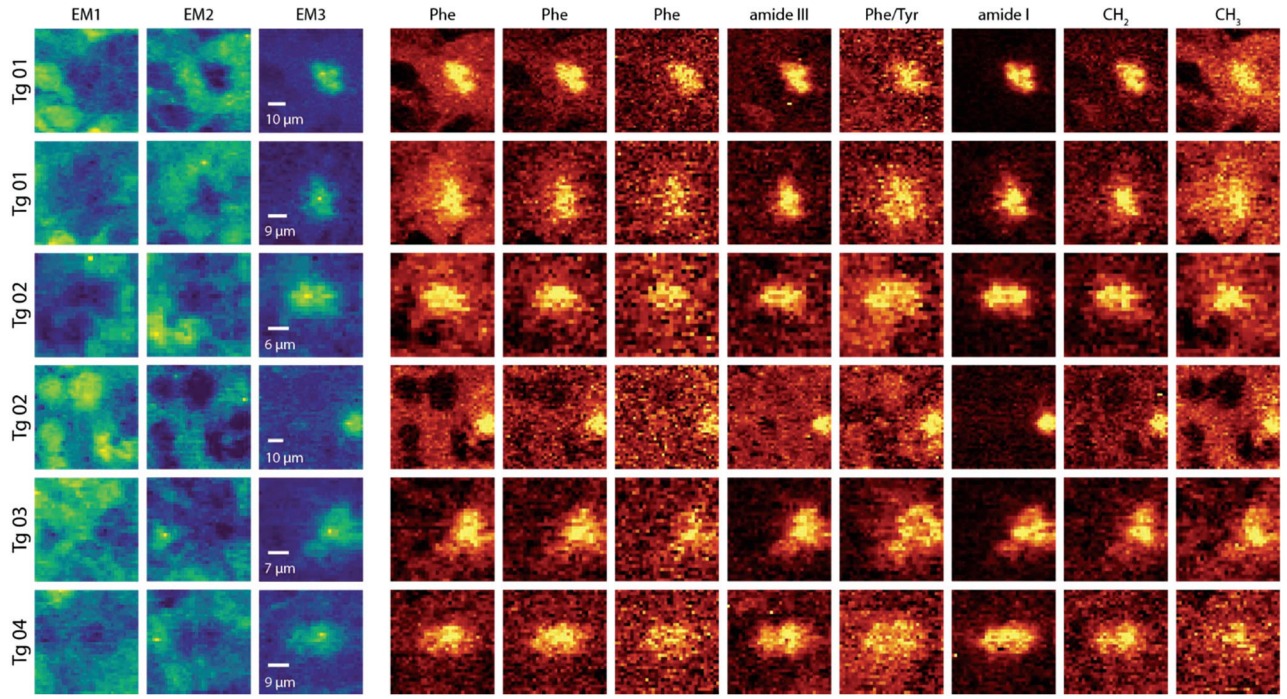

Fig. 3 Hyperspectral imaging of amyloid plaques. Raman spectroscopic mapping of four 6 month old transgenic mice (Tg01–Tg04) is represented here. Each row of images shows spectral imaging of one different amyloid plaque region. Each column represents different selected spectral information. The three first columns are obtained from the unsupervised spectral unmixing: EM1, background; EM2, the surrounding tissue; EM3, amyloid plaque spectral image. The next eight columns represent the intensity of scattered light in eight different spectral regions, obtained by selecting filters for each frequency in Project FIVE 5.0 WITec software. From left to right: Phe (1000–1012 cm^{-1}), Phe (1000–1040 cm^{-1}), Phe (1028–1043 cm^{-1}), amide III (1203–1263 cm^{-1}), Phe/Tyr (1604–1614 cm^{-1}), amide I (1670–1680 cm^{-1}), CH_2 (2869–2884 cm^{-1}), and CH_3 (2920–2940 cm^{-1}).

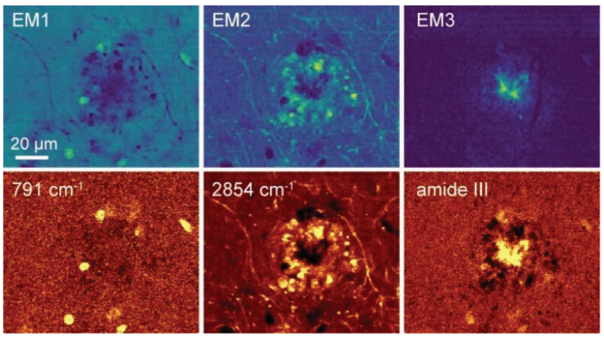

Fig. 4 High resolution hyperspectral imaging of amyloid plaques. Top – Results from the unsupervised spectral unmixing using 5 EMs: EM1, cell nucleus; EM2, the surrounding tissue; EM3, amyloid plaque spectral image. Two EMs (background and alternative plaque imaging) are not shown. Bottom – Analysis in WITec software selecting filters for DNA frequency (centered at 791 cm^{-1}), lipid (2854 cm^{-1}) and amide III (1203–1263 cm^{-1}).

biomarker of the protein secondary conformation in Raman spectroscopic analysis.[22,23,37] The β sheet secondary structure is assigned mainly to the C=O stretching vibration, which characterizes amide I (1670–1680 cm^{-1}). The 1672 cm^{-1} Raman peak related to the β sheet folding was confirmed here in the synthetic fibril samples (red trace in Fig. 1C), consistent with previous studies.[8,11,38] For a comparison purpose, the blue trace in Fig. 1C shows the Raman spectrum of BSA (majorly α helix),[17] exhibiting the amide I peak at 1658 cm^{-1}. In addition to amide I, the β sheet structure characterizing amyloid plaques show several other distinct characteristic vibration modes poorly explored. Among these, amide III is a complex vibration mode obtained from the sum of N–H bending and C–N stretching, and is influenced by (C)C_αH bending motion.[39] Data support amide III as the most sensitive vibration mode related to the peptide bond conformation in the secondary structure.[40] Besides, amide III in Aβ fibrils shows a band centered at ~1233 cm^{-1} (1203–1263 cm^{-1}) and a red-shift compared with BSA, which is centered at 1310 cm^{-1} (1280–1340 cm^{-1}). The spectra of both Aβ fibrils and BSA also showed the expected peaks of the phenylalanine (Phe) aromatic ring side chains (1004, 1032, 1609 cm^{-1}), tyrosine (Tyr, 1612 cm^{-1}),[41,42] and the CH_2 bending (δCH_2) vibration modes at 1452 cm^{-1}.[38]

Consistent with the results of the synthetic material, we observed in EM3 for tissues (Fig. 2E and G) the characteristic frequency shift in amide I, appearing centered at 1675 cm^{-1}, corresponding to the vibrational frequency of the β sheet secondary structure. These results support that the unsupervised analysis was able to accurately capture this spectral fingerprint in amyloid plaques, allowing the identification of further spectral features. We here point out four other Raman bands for

amyloid plaque identification, which are shown in the EM3 spectrum: Phe (1007–1036 cm^{-1}), amide III (1200–1330 cm^{-1}), Phe/Tyr (~1010 cm^{-1}) and CH stretching frequency (2800 to 3000 cm^{-1}). The Raman band intensity, which is attributed to Phe residues is increased at the amyloid plaque regions, probably due to the high concentration of these residues in Aβ peptides. The amide III region showed a red shift at the amyloid plaque compared to the surrounding tissue (Fig. 2E and F). This frequency mode is more complex than the others, since it involves a coupling of the Cα–H bending to the N–H in-plane-bending and the C–N stretching.[39] Furthermore, the CH stretching frequency mode showed a higher intensity near 2930 cm^{-1}, which is assigned to the higher concentration of the Aβ peptide at the plaques compared to the surrounding tissue. Therefore, the unsupervised spectral unmixing established the Raman fingerprint for amyloid plaque identification, obtained from amide I, amide III, Phe and CH stretching frequencies.

Hyperspectral imaging of amyloid plaques

Fig. 3 shows a combined set of spectral data obtained from different spectral regions of amyloid plaques. The six rows of images represent six different samples. In the first three columns, abundance mapping is shown in the function of the three end members, in which the brighter and spectrally more significant regions correspond to EM1 (first column), EM2 (second column) and EM3 (third column). Spectral unmixing is a statistical technique for the identification of specific spectra, which is used in the characterization of biological components in tissue ensembles.[29,43–45] As discussed in Fig. 2E, the EM3 image clearly shows the amyloid plaque, while EM2 highlights the surrounding tissue and EM1 the overall spectroscopic background. Guided by the different spectral features found in the EMs (Fig. 2), Fig. 3 displays, from the left to the right, the Raman intensity images in different spectral regions: Phe (1000–1012 cm^{-1}, 1000–1040 cm^{-1} and 1028–1043 cm^{-1}), amide III (1203–1263 cm^{-1}), Phe/Tyr (1604–1614 cm^{-1}), amide I (1670–1680 cm^{-1}), CH_2 (2877–2887 cm^{-1}), and CH_3 (2920–2940 cm^{-1}).

In all these regions, Raman spectra were able to properly detect and highlight amyloid plaques. Since the 1007 cm^{-1} peak of the Phe aromatic ring is one of the most intense bands in Raman spectra, the spectrum region from 1000 cm^{-1} to 1040 cm^{-1} was used to identify amyloid plaques with high contrast with the surrounding area. Another band related to Phe/Tyr at ~1610 cm^{-1} presented a similar effect in amyloid plaque identification. The amide III region centered at 1233 cm^{-1}, the amide I region at 1675 cm^{-1} and the region of higher frequency modes also highlighted plaques. The band centered at 2877 cm^{-1}, which is assigned to the CH_2 antisymmetric stretching vibrations of lipids and proteins,[46] produced a spectral image of the amyloid plaque that was sharper than that of the CH_3 symmetric stretching (2930 cm^{-1}).[26] Among CH frequencies, both have been associated with proteins and lipids; however, data suggest that the CH band presents higher accuracy in amyloid plaque identification.

Finally, Fig. 4 shows another set of hyperspectral Raman imaging performed in brain slices of older mice (12 months) with higher spatial resolution (500 nm step size) showing that the highest definition of the amyloid plaque demonstrates that Raman spectroscopy can be used for more complex compositional analysis. EM2 and EM3 describe the surrounding area and plaque core, respectively, while EM1 seems to highlight the cell nucleus. In the spectral image, DNA vibration (791 cm^{-1}), CH_2 symmetric stretching of the lipid (2854 cm^{-1}) and amide III frequencies reproduce the structures obtained in EM1, EM2 and EM3, respectively, showing that the precise limit of the plaque formed for the lipid-rich halo structure can be observed. Several spectroscopic studies with Raman and FTIR have demonstrated a region with lipid accumulation surrounding dense-core plaques forming the halo structure.[11,19,36,47–49]

No clear difference in the set of EM spectra was observed between 6 month and 12 month old mice. However, a longitudinal robust study is necessary for better characterization of the amyloid plaque difference between young and old transgenic mice.

Protein misfolding is a basic event in AD and other major neurodegenerative diseases, such as Parkinson and Huntington diseases, prion-related encephalopathies, and more than fifty other medical conditions.[50] In AD, amyloid plaque identification using positron emission tomography (PET) is a major complementary test in AD differential diagnosis. New radiotracers for PET have been able to mark amyloid plaques and tau tangles in AD patients.[51,52] However, PET imaging is an expensive technique which presents limited accuracy in early AD. The definite diagnosis of AD still relies on histopathological staining using Congo red,[53] which represents the gold standard diagnostic biomarker for AD *post mortem* diagnosis. Raman spectroscopy is pointed here as an inexpensive non-invasive early diagnostic technique enabling *in vivo* intraocular amyloid plaque identification.

Previous Raman studies were performed using Aβ synthetic peptides,[9] Aβ peptide inoculation into rat brains, and different spectroscopic methods and protocols, including distinct procedures for sample preparation, as fresh or cryosectioning slices.[10,11,19,36] In this study, we describe an unbiased statistical modelling analysis of the hyperspectral Raman data of amyloid plaques and surrounding tissues, as well as perform imaging using different spectral signatures. The identification of the different spectral features allowed a more reliable spectral identification protocol which provides tools to better understand the complexity of biochemical and pathophysiological events that take place in neurodegenerative diseases, especially AD.

In both synthetic fibrils and amyloid plaques, the amide III band can be used, in addition to amide I, as an accurate Raman fingerprint for Aβ peptide identification. This is supported by studies that demonstrate the sensitivity of amide III to identify the Aβ backbone conformation.[39,54–57] For both the Aβ synthetic fibrils (Fig. 1C) and the amyloid plaque tissue (Fig. 2F), a similar red-shift is observed. It is important to highlight that the broad amine III Raman profile harbors various other vibrational modes related to several bio-

molecules, like DNA, phosphodiester groups in nucleic acids, stretching of C–N, CH bending of lipids, triglycerides, CH_2 in-plane deformation, and typical phospholipids.[7] Despite its complexity, the shift related to the β conformation of the protein, as shown in Fig. 2F, is prominent.

In the amide I spectral region, we observed a frequency shift as high as 1672 cm^{-1}, with the maximum at 1675 cm^{-1}, whereas the spectra remained at around 1665 cm^{-1} in the surrounding tissue. Therefore, when prominent, the blue-shift in amide I comes together with the red-shift in amide III, as discussed above. We presented three spectra of Phe in the Aβ peptide, as well as their distribution in the plaque (Fig. 2 and 3). For the CH_2 stretching, the frequency centered at 2877 cm^{-1} (Fig. 3) displays the amyloid plaque spectral image with appropriate spatial resolution and contrast, as with the amide III band. By combining the hyperspectral Raman imaging and the spectral unmixing statistical method, we were able to obtain the most distinct set of spectra in a complex ensemble in neural tissues. Therefore, these spectra can be used as a robust multifrequency spectral fingerprint of the amyloid plaques and the surrounding tissue.

Conclusions

In this study, hyperspectral Raman imaging and spectral unmixing were achieved in synthetic fibrils and neural tissues from an AD model of bitransgenic $APP_{swe}PS1_{\Delta E9}$ mice, with the aim to characterize amyloid plaques. The high spectral and spatial resolution of Raman spectroscopy allowed us to distinguish the β sheet fibril structures of the amyloid plaques from the surrounding tissues. The spectral unmixing method relies on the overall spectral differences in order to find distinct spectral signatures, thus providing a robust method of plaque identification, enabling further histological examination and characterization of hallmarks of β sheet-related neurodegenerative disorders.

Recent results have shown that it is possible to find amyloid plaques in the retina.[14,58,59] For establishing Raman spectroscopy as a diagnosis method, laser power and wavelength are important aspects to be considered for defining the measurement protocol. It is possible that the use of a defocussed light source and stimulated Raman[11] may be needed. The need to scan larger areas of the tissue to find plaques, and the possible differences in autofluorescence of the live retinal tissue are challenges to be addressed in future studies. Anyhow, the comprehensive multi-frequency spectral understanding that we have established here provides a complete fingerprint to guide future work in this field.

Methods

In vitro Aβ experiments

The $A\beta_{1-42}$ synthetic peptide was purchased from Geneone (Rio de Janeiro). Before the fibril formation procedure, we standardized the monomerization process of the peptide, using 1,1,1,3,3,3-hexafluoro-2-propanol. The peptide was solubilized with 10 μL of 100 mM NaOH solution and diluted in ultrapure water to a 200 μM final concentration. The pH value was set to 7.8 and the final solution was incubated at 37 °C for 48 h to allow fibril formation.[16] A drop of Aβ fibrils was deposited onto glass cover slips and dried in air at room temperature. Bovine serum albumin (1 mg mL^{-1}) was deposited onto glass cover slips for Raman spectra acquisition.

Animal model

Six- and twelve-month old double transgenic mice (Tg) $APP_{swe}PS1_{\Delta E9}$ bearing a chimeric human/mouse $APP_{swe}PS1_{\Delta E9}$ mutation (Jackson Laboratory) were used in this study. These double transgenic mice show increased and early Aβ deposition in the brain after 5 months of age.[60–62] Our investigation was in accordance with the Guide for the Care and Use of Laboratory Animals and approved by the Ethics Committee for Animal Utilization in Research (CEUA) of the Federal University of Minas Gerais (protocol 225/2014), under the criteria of the National Animal Experimentation Control Council (CONCEA).

Tissue preparation

Four Tg mice (6 months) were perfused transcardially with ice-cold phosphate-buffered saline (PBS) followed by 4% paraformaldehyde (PFA) in PBS (pH 7.4). Brains were removed and kept overnight in 4% PFA for complete fixation. Afterwards, they were embedded in the O.C.T. compound (Fisher Healthcare) followed by coronary cryosectioning of the frontal cortex and hippocampus (80 μm). Serial tissue sections were washed three times for 15 minutes with PBS to remove the O.C.T. compound completely, avoiding spectral interference. Slices of an additional Tg mouse (12 months) were analyzed using a vibrating 330 blade microtome (Leica Microsystems; Wetzlar, Hesse, Germany).

Thioflavin S staining

Tissue sections were stained using 1% ThioS solution (w/v) in 70% ethanol (v/v) (Sigma-Aldrich). Briefly, samples were immersed for 10 minutes in ThioS solution, immediately dipped three times in 70% ethanol, and washed with PBS and seeded directly on coverslips. Subsequently, fluorescence images were obtained.

Fluorescence microscopy

Autofluorescence imaging was performed before Raman spectroscopic measurements and Thioflavin S (ThioS) fluorescence was measured after the Raman spectroscopic measurements. Autofluorescence and fluorescence imaging was performed by two-photon-excited fluorescence (TPEF) microscopy. An inverted Nikon laser scanning microscope (Lavision Biotec) with an 80 MHz, 7 picosecond laser (APE PicoEmerald) centered at 830 nm was used for TPEF. A GaAsP photomultiplier with a bandpass filter of 525/40 nm was used as the detector.

Transmission electronic microscopy

Samples were diluted 10×, deposited onto carbon-coated copper mesh grids and negatively stained with 2% (w/v) uranyl

acetate. The fibrils were imaged with a Tecnai G2-12-FEI SpiritBiotwin 120 kV Camera CCD Mega View III.

Atomic force microscopy

Atomic force microscopy (AFM) images were acquired in the tapping mode with a NanoWizard BioScience Atomic Force Microscope (JPK Instruments). The samples were placed onto clean glass substrates and dried under a gentle nitrogen flow.

Raman spectroscopy

A confocal Raman Microscope WITec Alpha 300 SAR was used for Raman spectroscopy and imaging. All measurements were performed with 532 nm excitation. For the Aβ fibril deposited sample, a 50× (0.55 NA) objective was used and the spectra were integrated for 5 × 5 s, excited with 5 mW laser power. For Raman mapping, data were collected at 1 s dwell time per pixel every 1.2 μm step, at 20 mW laser power. For 12 month old Tg mice, the data were collected with 0.5 s dwell time per pixel and 0.5 μm steps. The sum of the acquired spectra for the end member analysis shown here was 55 051, with plaque imaging ranging from 25 × 25 to 220 × 198 hyperspectra. However, in total, more than 87 811 spectra were measured and analyzed, providing consistent results (not shown).

Data analysis and processing or cluster analysis

A supervised method was used for image generation using Project FIVE 5.0 WITec software. All hyperspectral data were submitted to the unsupervised unmixing software using N-FINDR and FCLS (Fully Constrained Least Squares) algorithms,[29,44] which decompose the collection of constituent spectra in end members (EMs), as well as their corresponding fractions (abundances) that indicate the proportion of each endmember in the pixel.[63] EM spectra were plotted using OriginPro software.

Author contributions

E.A.F. contributed to the acquisition, analysis, and interpretation of the data and wrote the paper. L.L. and R.C. developed the two-photon system and collected the data. H.M. and J.C. developed the unmixing software and analyzed the data. H.G. M. performed the AFM. M.R.S. provided the very early conceptual idea and contributed to the establishment of the colony of mice. R.A.S., A.S.B. and R.P.V. contributed to the scientific interpretation of the data and significantly revised the article. L.M.M. and A.J. contributed to the conception and design of the work and substantively revised the article. All authors read and approved the submitted version of the article.

Conflicts of interest

The authors declare non-financial interest in relation to the work described here.

Acknowledgements

We acknowledge Cassiano Rabelo for the technical help. Raman analysis was performed at LabNS and LCPNano, Physics Department, UFMG. Electron microscopy analysis was performed at the UFMG Microscopy Center. This work was financed by the Brazilian Agency FINEP (contract no. 01.13.0330.00) and FAPEMIG (Rede Mineira).

References

1 D. J. Selkoe, *Physiol. Rev.*, 2001, **81**, 741–767.
2 B. Olsson, *Lancet Neurol.*, 2016, **15**, 673–684.
3 B. Frisoni, M. Boccardi, F. Barkhof, K. Blennow, S. Cappa, K. Chiotis, *et al.*, *Lancet Neurol.*, 2017, **16**, 661–676.
4 D. J. Selkoe and J. Hardy, *EMBO Mol. Med.*, 2016, **8**, 595–608.
5 N. Amharref, A. Beljebbar, S. Dukic, L. Venteo, L. Schneider, M. Pluot and M. Manfait, *Biochim. Biophys. Acta*, 2007, **1768**, 2605–2615.
6 J. Dybas, K. M. Marzec, M. Z. Pacia, K. Kochan, K. Czamara, K. Chrabaszcz, E. Staniszewska-Slezak, K. Malek, M. Baranska and A. Kaczor, *TrAC, Trends Anal. Chem.*, 2016, **85**, 117–127.
7 Z. Movasaghi, S. Rehman and I. U. Rehman, *Appl. Spectrosc. Rev.*, 2007, **42**, 493–541.
8 J. Dong, C. S. Atwood, V. E. Anderson, S. L. Siedlak, M. A. Smith, G. Perry and P. R. Carey, *Biochemistry*, 2003, **42**, 2768–2773.
9 P. Chen, A. Shen, W. Zhao, S. L. Baek, H. Yuan and J. Hu, *Appl. Opt.*, 2009, **48**, 4743–4748.
10 R. Michael, A. Lenferink, G. F. J. M. Vrensen, E. Gelpi, R. I. Barraquer and C. Otto, *Sci. Rep.*, 2017, **7**, 1–11.
11 M. Ji, M. Arbel, L. Zhang, C. W. Freudiger, S. S. Hou, D. Lin, X. Yang, B. J. Bacskai and X. S. Xie, *Sci. Adv.*, 2018, **4**, eaat7715.
12 M. Koronyo-Hamaoui, Y. Koronyo, A. V. Ljubimov, C. A. Miller, M. K. Ko, K. L. Black, M. Schwartz and D. L. Farkas, *NeuroImage*, 2011, **54**, S204–S217.
13 M. Rafii, H. Wishnek, J. B. Brewer, M. C. Donohue, S. Ness, W. C. Mobley, P. S. Aisen and R. A. Rissman, *Front. Behav. Neurosci.*, 2015, **9**, 1–11.
14 Y. Koronyo, D. Biggs, E. Barron, D. S. Boyer, J. A. Pearlman, W. J. Au, S. J. Kile, A. Blanco, D. T. Fuchs, A. Ashfaq, S. Frautschy, G. M. Cole, C. A. Miller, D. R. Hinton, S. R. Verdooner, K. L. Black and M. Koronyo-Hamaoui, *JCI Insight*, 2017, **2**, 1–19.
15 S. E. Perez, S. Lumayag, B. Kovacs, E. J. Mufson and S. Xu, *Invest. Ophthalmol. Visual Sci.*, 2009, **50**, 793–800.
16 M. Ahmed, J. Davis, D. Aucoin, T. Sato, S. Ahuja, S. Aimoto, J. I. Elliott, W. E. Van Nostrand and S. O. Smith, *Nat. Struct. Mol. Biol.*, 2010, **17**, 561–567.
17 V. J. C. Lin and J. L. Koenig, *Biopolymers*, 1976, **15**, 203–218.
18 A. C. Kwan, K. Duff, G. K. Gouras and W. W. Webb, *Opt. Express*, 2009, **17**, 3679–3689.

19 K. L. Summers, N. Fimognari, A. Hollings, M. Kiernan, V. Lam, R. J. Tidy, D. Paterson, M. J. Tobin, R. Takechi, G. N. George, I. J. Pickering, J. C. Mamo, H. H. Harris and M. J. Hackett MJ, *Biochemistry*, 2017, **56**, 4107–4116.
20 G. M. Shankar, S. Li, T. H. Mehta, A. Garcia-Munoz, N. E. Shepardson, I. Smith, F. M. Brett, M. A. Farrell, M. J. Rowan, C. A. Lemere, C. M. Regan, D. M. Walsh, B. L. Sabatini and D. J. Selkoe, *Nat. Med.*, 2008, **7**, 3374.
21 M. Jin, N. Shepardson, T. Yang, G. Chen, D. Walsh and D. J. Selkoe, *Proc. Natl. Acad. Sci. U. S. A.*, 2011, **108**, 5819–5824.
22 A. Barth and C. Zscherp, *Q. Rev. Biophys.*, 2002, **35**, 369–430.
23 A. Rygula, K. Majzner, K. M. Marzec, A. Kaczor, M. Pilarczyk and M. Baranska, *J. Raman Spectrosc.*, 2013, **44**, 1061–1076.
24 S. Krimm and J. Bandekar, *Adv. Protein Chem.*, 1986, **38**, 181–364.
25 J. L. Lippert, D. Tyminski and P. J. Desmeules, *J. Am. Chem. Soc.*, 1976, **98**, 7075–7080.
26 C. Krafft, L. Neudert, T. Simat and R. Salzer, *Spectrochim. Acta, Part A*, 2005, **61**, 1529–1535.
27 K. Czamara, K. Majzner, M. Z. Pacia, K. Kochan, A. Kaczor and M. Baranska, *J. Raman Spectrosc.*, 2014, **46**, 4–20.
28 M. Daković, *et al.*, *Talanta*, 2013, **117**, 133–138.
29 N. Bergner, C. Krafft, K. D. Geiger, M. Kirsch, G. Schackert and J. Popp, *Anal. Bioanal. Chem.*, 2012, **403**, 719–725.
30 S. D. Moran and M. T. Zanni, *J. Phys. Chem.*, 2014, **5**, 1984–1993.
31 A. Barth, *Prog. Biophys. Mol. Biol.*, 2000, **74**, 141–173.
32 O. Klementieva, K. Willén, I. Martinsson, B. Israelsson, A. Engdahl, J. Cladera, P. Uvdal and G. K. Gouras, *Nat. Commun.*, 2017, **8**, 14726.
33 M. Z. Kastyak-Ibrahim, M. J. Nasse, M. Rak, C. Hirschmugl, M. R. Del Bigio, B. C. Albensi and K. M. Gough, *NeuroImage*, 2012, **60**, 376–383.
34 M. J. Hackett, J. A. McQuillan, F. El-Assaad, J. B. Aitken, A. Levina, D. D. Cohen, R. Siegele, E. A. Carter, G. E. Grau, N. H. Hunt and P. A. Lay, *Analyst*, 2011, **136**, 2941–2952.
35 K. Kochan, K. Chrabaszcz, B. Szczur, E. Maslak, J. Dybas and K. M. Marzec, *Analyst*, 2016, **141**, 5329–5338.
36 F. Palombo, F. Tamagnini, J. C. G. Jeynes, S. Mattana, I. Swift, J. Nallala, J. Hancock, J. T. Brown, A. D. Randall and N. Stone, *Analyst*, 2018, **143**, 850–857.
37 J. Bandekar, *Biochim. Biophys. Acta, Protein Struct. Mol. Enzymol.*, 1992, **1120**, 123–143.
38 Z. Krištofiková, V. Kopecký, K. Hofbauerová, P. Hovorková and D. Řípová, *Neurochem. Res.*, 2008, **33**, 412–421.
39 S. A. Asher, A. Ianoul, G. Mix, M. N. Boyden, A. Karnoup, M. Diem and R. Schweitzer-Stenner, *J. Am. Chem. Soc.*, 2001, **123**, 11775–11781.
40 A. V. Mikhonin, Z. Ahmed, A. Ianoul and S. A. Asher, *J. Phys. Chem.*, 2004, **108**, 19020–19028.
41 B. Sjöberg, S. Foley, B. Cardey and M. Enescu, *Spectrochim. Acta, Part A*, 2014, **128**, 300–311.
42 T. Pazderka and V. Kopecký, *Spectrochim. Acta, Part A*, 2017, **185**, S1–S4.
43 T. W. Bocklitz, S. Guo, O. Ryabchykov, N. Vogler and J. Popp, *Anal. Chem.*, 2016, **88**, 133–151.
44 M. Hedegaard, C. Matthäus, S. Hassing, C. Krafft, M. Diem and J. Popp, *Theor. Chem. Acc.*, 2011, **130**, 1249–1260.
45 C. Kallepitis, M. S. Bergholt, M. M. Mazo, V. Leonardo, S. C. Skaalure, S. A. Maynard and M. M. Stevens, *Nat. Commun.*, 2017, **8**, 14843.
46 R. G. Snyder, S. L. Hsu and S. Krimm, *Spectrochim. Acta, Part A*, 1978, **34**, 395–406.
47 M. Rak, M. R. Del Bigio, S. Mai and D. G. K. Westaway, *Biopolymers*, 2007, **86**, 345–347.
48 C. R. Liao, *et al.*, *Analyst*, 2013, **138**, 3991–3997.
49 R. J. Tidy, V. Lam, N. Fimognari, J. C. Mamo and M. J. Hackett, *Vib. Spectrosc.*, 2017, **91**, 68–76.
50 T. P. J. Knowles, M. Vendruscolo and C. M. Dobson, *Nat. Rev. Mol. Cell Biol.*, 2014, **15**, 384–396.
51 L. Yang, D. Rieves and C. Ganley, *N. Engl. J. Med.*, 2010, **367**, 885–887.
52 H. Zetterberg and J. M. Schott, *Nat. Med.*, 2019, **25**, 201–203.
53 P. Frid, S. V. Anisimov and N. Popovic, *Brain Res. Rev.*, 2007, **53**, 135–160.
54 K. Kaiden, T. Matsui and S. Tanaka, *Appl. Spectrosc.*, 1987, **41**, 180–184.
55 I. H. McColl, E. W. Blanch, A. C. Gill, A. G. Rhie, M. A. Ritchie, L. Hecht, K. Nielsen and L. D. Barron, *J. Am. Chem. Soc.*, 2003, **125**, 0–7.
56 S. Cai and B. R. Singh, *Biochemistry*, 2004, **43**, 2541–2549.
57 J. Huang, K. Tian, S. Ye and Y. Luo, *J. Phys. Chem.*, 2016, **120**, 15322–15328.
58 S. S. More and R. Vince, *ACS Chem. Neurosci.*, 2015, **6**, 306–315.
59 X. Hadoux, *Nat. Commun.*, 2019, **10**, 4227.
60 D. R. Borchelt, T. Ratovitski, J. van Lare, M. K. Lee, V. Gonzales, N. A. Jenkins, N. G. Copeland, D. L. Price and S. S. Sisodia, *Neuron*, 1997, **19**, 939–945.
61 J. L. Jankowskya, H. H. Slunta, T. Ratovitskia, N. A. Jenkinsc, N. G. Copelandc and D. R. Borchelta, *Biomol. Eng.*, 2001, **17**, 157–165.
62 M. Garcia-Alloza, E. M. Robbins, S. X. Zhang-Nunes, S. M. Purcell, R. A. Betensky, S. Raju, C. Prada, S. M. Greenberg, B. J. Bacskai and M. P. Frosch, *Neurobiol. Dis.*, 2006, **24**, 516–524.
63 N. Keshava and J. F. Mustard, *IEEE Signal Process. Mag.*, 2002, **19**, 44–57.

